
NeRF-VAE: A Geometry Aware 3D Scene Generative Model

Adam R. Kosiosek^{*1} Heiko Strathmann^{*1} Daniel Zoran¹ Pol Moreno¹ Rosalia Schneider¹ Soňa Mokrá¹
 Danilo J. Rezende¹

Abstract

We propose NeRF-VAE, a 3D scene generative model that incorporates geometric structure via Neural Radiance Fields (NeRF) and differentiable volume rendering. In contrast to NeRF, our model takes into account shared structure across scenes, and is able to infer the structure of a novel scene—without the need to re-train—using amortized inference. NeRF-VAE’s explicit 3D rendering process further contrasts previous generative models with convolution-based rendering which lacks geometric structure. Our model is a VAE that learns a distribution over radiance fields by conditioning them on a latent scene representation. We show that, once trained, NeRF-VAE is able to infer and render geometrically-consistent scenes from previously unseen 3D environments using very few input images. We further demonstrate that NeRF-VAE generalizes well to out-of-distribution cameras, while convolutional models do not. Finally, we introduce and study an attention-based conditioning mechanism of NeRF-VAE’s decoder, which improves model performance.

1 Introduction

The ability to infer the structure of scenes from visual inputs, and to render high quality images from different viewpoints, has vast implications for computer graphics and virtual reality.

This problem has traditionally been tackled with 3D reconstruction-based on matching visual keypoints, e. g. Lowe (2004); Schönberger & Frahm (2016). While these methods incorporate structure through multi-view geometry (Hartley & Zisserman, 2003), very few existing methods adopt learned scene-priors such as types of objects or statistics of the background. The resulting representations are usually discrete: they consist of meshes (Dai et al., 2017),

^{*}Equal contribution, random order ¹DeepMind, London. Correspondence to: ARK <adamrk@google.com>, HS <strathmann@google.com>.

point clouds (Engel et al., 2014), or discretized volumes (Ulusoy et al., 2016), and are difficult to integrate with neural networks. An alternative approach to scene generation uses light-field rendering (Levoy & Hanrahan, 1996; Srinivasan et al., 2017) and multiplane image representations (Zhou et al., 2018; Mildenhall et al., 2019). While these methods allow image-based rendering, they do not estimate scene geometry. Hence, they are not directly useful for the purpose of 3D scene understanding. More recent deep-learning-based novel view synthesis methods have the advantages of end-to-end training, and producing distributed representations that can be easily used in other neural-net-based downstream tasks. These models, however, often have little embedded geometrical knowledge (Dosovitskiy et al., 2014) and are either geometrically inconsistent (Nguyen-Phuoc et al., 2020) or provide insufficient visual quality (Tatarchenko et al., 2015). Moreover, many of these methods are deterministic and cannot manage uncertainty in the inputs (Sitzmann et al., 2019; Trevithick & Yang, 2021).

This work attempts to address these shortcomings. We introduce NeRF-VAE—a deep generative model with the knowledge of 3D geometry as well as complex scene priors. Our work builds on Neural Radiance Fields (NeRF, Mildenhall et al. (2020)). NeRF combines implicit neural network representations of radiance fields, or *scene functions*, with a volumetric rendering process. NeRF needs to undergo a lengthy optimization process on many views of each single scene separately and does not generalize to novel scenes. In contrast, NeRF-VAE—a variational auto-encoder (VAE)—models multiple scenes, while its constant-time amortized inference allows reasoning about novel scenes. Unlike NeRF, our model is also generative, and therefore capable of handling missing data and imagining completely new scenes. In that, our work closely follows Generative Query Networks (GQN, Eslami et al. (2018)). Like GQN, NeRF-VAE defines a distribution over scene functions. Once sampled, a scene function allows rendering arbitrary views of the underlying scene. Where GQN relies on convolutional neural networks (CNNs) with no knowledge of 3D geometry, leading to geometrical inconsistencies, NeRF-VAE achieves consistency by leveraging NeRF’s implicit representations and volumetric rendering.

NeRF represents a scene by the values of multilayer percep-

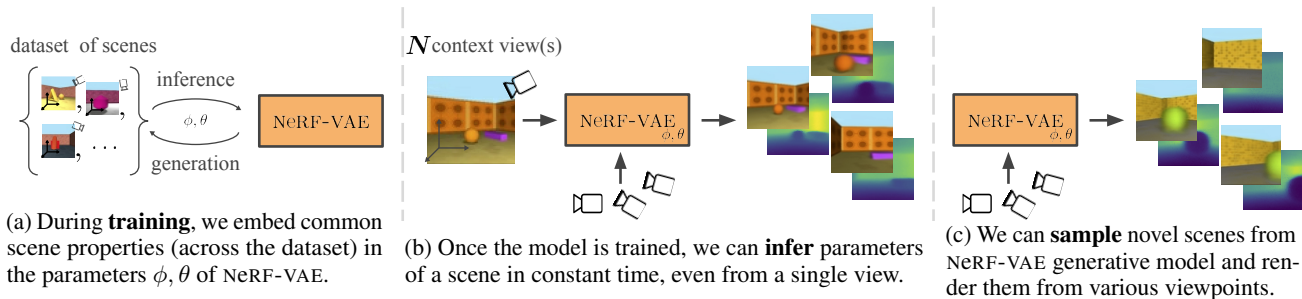


Figure 1: An overview of NeRF-VAE: a geometry-aware 3D scene generative model. NeRF-VAE is trained on a dataset of several views (images and camera positions/orientations) from **multiple scenes**. Once trained, it allows for efficient inference of scene parameters (colours and geometry, including depth-maps) and sampling novel scenes from the prior.

tron (MLP) parameters. Being extremely high-dimensional, this representation precludes using amortized inference. We change NeRF’s formulation to a scene function shared between scenes, and conditioned on a **per-scene** latent variable. Intuitively, the latent variable captures scene-specific information (e. g. position and kind of objects, colours, lighting, etc.), while shared information (e. g. available textures and shapes, properties of common elements, sky) is stored in the parameters of the scene function. A prior over latent variables (and therefore scene functions) allows sampling novel scenes from the model, and rendering arbitrary viewpoints within them. NeRF-VAE parameters are learned using a collection of images from different scenes, with known camera position and orientation. Since these parameters are shared between scenes (unlike in NeRF), NeRF-VAE can infer scene structure from very few views of an unseen scene. This is in contrast to NeRF, where using few views results in poor performance. A high level overview of NeRF-VAE is depicted in Fig. 1.

In summary, NeRF-VAE introduces four key benefits compared to existing models. First, due to its amortized inference, it removes the need for costly optimization from scratch for every new scene. Second, as it learns shared information between multiple scenes, it is able reconstruct unobserved scenes from a much smaller number of input views. Third, compared to existing convolutional generative models for view synthesis, such as GQN, it generalizes much better when evaluated on out-of-distribution camera views. Finally, NeRF-VAE is the only amortized NeRF variant that uses compact scene representation in the form of a latent variable and that can handle uncertainty in the inputs.

2 Neural Radiance Fields (NeRF)

NeRF’s scene function is represented as a 6D continuous vector-valued function whose inputs are ray coordinates (\mathbf{x}, \mathbf{d}) partitioned into position $\mathbf{x} \in \mathbb{R}^3$ and orientation¹

¹It is also possible to parameterize orientation using two angles, as e. g. done by Mildenhall et al. (2020), but we follow their

$\mathbf{d} \in \mathbb{R}^3$. Its outputs are an emitted colour $(r, g, b) \in \mathbb{R}^3$ and a volume density $\sigma \geq 0$. The scene function is approximated by a neural network $F_\theta : (\mathbf{x}, \mathbf{d}) \mapsto ((r, g, b), \sigma)$ with weights θ . In order to encourage multi-view consistency, the architecture of this network is such that volume density σ only depends on position while the emitted colour (r, g, b) depends on both position and ray orientation.

Volumetric image rendering works by casting rays from the camera’s image plane into the scene, one ray per pixel. The colour that each ray produces is the weighted average of colours along the ray, with weights given by their accumulated volume densities. NeRF’s renderer uses a differentiable approximation to this accumulation process. For details, we refer to Mildenhall et al. (2020); Curless & Levoy (1996).

We denote the image rendering process whose inputs are a **camera** \mathbf{c} (position and orientation) and a scene function F_θ , and which outputs the rendered image² $\hat{\mathbf{I}}$, by

$$\hat{\mathbf{I}} = \text{render}(F_\theta(\cdot), \mathbf{c}). \quad (1)$$

Note that computation of the camera’s image plane and corresponding rays for each pixel requires camera parameters (e. g. field of view, focal length, etc).

3 NeRF-VAE

We build a generative model over scenes by introducing a view-independent latent variable \mathbf{z} with prior $p(\mathbf{z})$ and a **conditional scene function** $G_\theta(\cdot, \mathbf{z}) : (\mathbf{x}, \mathbf{d}) \mapsto ((r, g, b), \sigma)$. G_θ is much like NeRF’s F_θ , but is additionally conditioned on \mathbf{z} , as will be detailed in Section 3.2.

It is now the latent variable \mathbf{z} that defines a **specific** scene, out of all the scenes that G_θ is able to represent, where θ are model parameters that capture **shared structure** across scenes. The generative process of NeRF-VAE involves sampling $\mathbf{z} \sim p(\mathbf{z})$ and using the resulting con-

²Note that it is easily possible to compute depth estimates for each rendered ray. We use this for visualization and evaluation purposes.

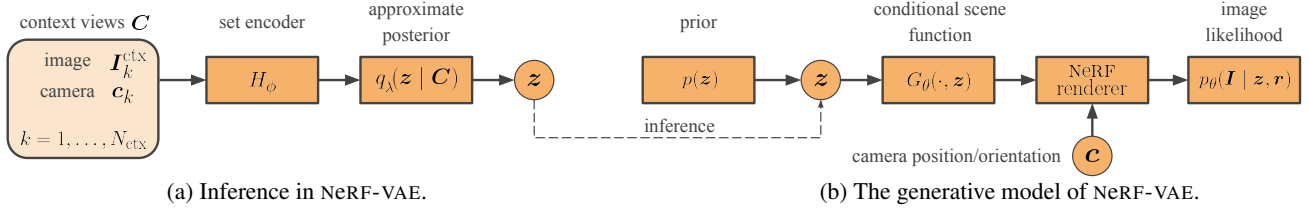


Figure 2: Inference and generative model of NeRF-VAE. For inference, a set \mathcal{C} of context images $\mathbf{I}_k^{\text{ctx}}$ and cameras \mathbf{c}_k from a scene are encoded into an approximate posterior distribution over the latent variable \mathbf{z} . This conditions a scene function $G_\theta(\cdot, \mathbf{z})$, which is used by the NeRF renderer to reconstruct images from arbitrary cameras within the scene. We can sample novel scenes by sampling the latent \mathbf{z} from the prior. During training, the reconstruction MSE and the KL divergence are used in a variational optimization objective to learn the parameters θ of the conditional scene function and the parameters ϕ of the encoder.

ditional scene function $G_\theta(\cdot, \mathbf{z})$ to render an image $\hat{\mathbf{I}} = \text{render}(G_\theta(\cdot, \mathbf{z}), \mathbf{c})$ from a camera \mathbf{c} with volumetric rendering from Eq. (1).

The individual pixel colours $\hat{\mathbf{I}}(i, j)$ are used to define the mean parameter of a Gaussian image likelihood

$$p_\theta(\mathbf{I} | \mathbf{z}, \mathbf{c}) = \prod_{i,j} \mathcal{N}(\mathbf{I}(i, j) | \hat{\mathbf{I}}(i, j), \sigma_{\text{lik}}^2)$$

with fixed or learned variance σ_{lik}^2 , and we assume conditional independence of individual pixels $\mathbf{I}(i, j)$ given \mathbf{z} .

Since the posterior over \mathbf{z} is intractable, we approximate it—we frame NeRF-VAE as a variational auto-encoder (VAE, Kingma & Welling (2014); Rezende et al. (2014)) with **conditional** NeRF as its decoder.

3.1 Amortized Inference for NeRF-VAE

Estimating the scene function parameters in NeRF is done separately for every scene, with no information sharing between scenes, which is time-consuming, compute-intensive, and data-hungry.

In contrast, NeRF-VAE introduces an encoder network E_ϕ with parameters ϕ , which amortizes inference of the latent variable \mathbf{z} . Input for the encoder is a collection of N_{ctx} **context views**, where each view consists of an image $\mathbf{I}^{\text{ctx}} \in \mathbb{R}^{H \times W \times 3}$ and corresponding camera position and orientation \mathbf{c} . These views correspond to different viewpoints of a particular scene, forming a context set $\mathcal{C} := \{\mathbf{I}_k^{\text{ctx}}, \mathbf{c}_k\}_{k=1}^{N_{\text{ctx}}}$. Each context element (concatenated camera \mathbf{c}_k with image $\mathbf{I}_k^{\text{ctx}}$) is separately encoded using a shared encoder—we use a ResNet adapted from Vahdat & Kautz (2020), details in Appendix B. The resulting N_{ctx} outputs are subsequently averaged³ and mapped to parameters λ of the approximate posterior distribution $q_\lambda(\mathbf{z} | \mathcal{C})$ over the latent variable \mathbf{z} . We use diagonal Gaussian posteriors.

³We choose this method for its conceptual simplicity and note that more sophisticated options, such as attention-based mechanisms, might lead to better results as in Trevithick & Yang (2021)—exploration of which we leave for future work.

We fit the parameters $\{\theta, \phi\}$ of the NeRF-VAE by maximizing the following evidence lower bound (ELBO) on images,

$$\mathcal{L}_{\text{NeRF-VAE}}(\mathbf{I}, \mathbf{c}, \mathcal{C}; \theta, \phi) = \mathbb{E}_{\mathbf{z} \sim q} [\log p_\theta(\mathbf{I} | \mathbf{z}, \mathbf{c})] - \text{KL}(q_\lambda(\mathbf{z} | \mathcal{C}) || p(\mathbf{z})). \quad (2)$$

In practice, we approximate the ELBO by uniformly subsampling pixels from each image, see Appendix D for details.

Iterative Amortized Inference Amortized inference suffers from *amortization gap* (Cremer et al., 2018)—contrasting the gradient-based learning in NeRF. To bridge this gap, we employ iterative (amortized) inference (Kim et al., 2018; Marino et al., 2018), which trades-off additional compute for improved inference.

Iterative inference starts with an arbitrary guess for the posterior parameters, e. g. $\lambda_0 = \mathbf{0}$, and iteratively refines them. At each step t , a latent is sampled from the current posterior $\mathbf{z} \sim q_{\lambda_t}(\mathbf{z} | \mathcal{C})$. The sample is then used to render an image and to evaluate the gradient of the ELBO in Eq. (2) w. r. t. λ_t . The gradient is passed to a recurrent refinement network (LSTM followed by a linear layer)⁴ f_ϕ , which updates the posterior parameters λ_t for a given \mathcal{C} :

$$\begin{aligned} \mathbf{z}_t &\sim q_{\lambda_t}(\mathbf{z} | \mathcal{C}), \\ \lambda_{t+1} &\leftarrow \lambda_t + f_\phi(E_\phi(\mathcal{C}), \nabla_{\lambda_t} \mathcal{L}_{\text{NeRF-VAE}}). \end{aligned}$$

See Appendix B for further details.

We emphasize that NeRF-VAE’s decoder uses explicit geometric structure, which consequently is used by iterative inference. While this is only in an implicit manner (through ELBO gradients), it differs from a geometry-agnostic feed-forward encoder typically used with VAEs.

3.2 Conditioning the Scene Function

We now describe NeRF-VAE’s conditional scene function $G_\theta(\cdot, \mathbf{z})$, which is conditioned on the per-scene latent variable \mathbf{z} and has additional across-scene parameters θ .

⁴Note that in this case, ϕ only contains parameters of the context encoder E_ϕ as well as the refinement network.

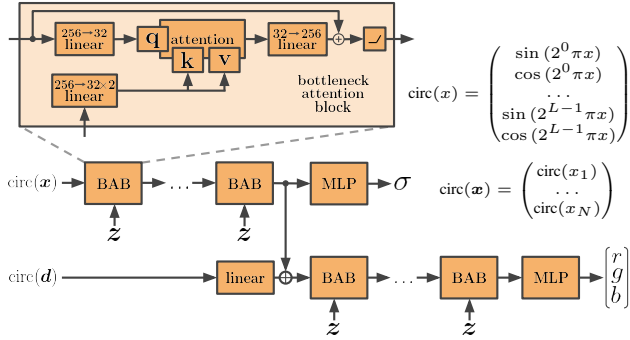


Figure 3: Attention-based scene function. Input points (\mathbf{x}, \mathbf{d}) , along rays corresponding to each pixel in the camera plane, **attend** to different locations of the spatial latent variable \mathbf{z} of size $[H_z \times W_z \times D_z]$ using multi-head attention. The density part (σ) depends only on the position \mathbf{x} as in NeRF. Each attention block receives a different slice of the latent along its channel dimension. The inputs are projected to a lower-dimension space to save computation and memory; \oplus is concatenation.

A simple way to condition NeRF’s scene function MLP is to use \mathbf{z} to shift and scale the inputs and activations at different layers—this mechanism resembles AIN of Dumoulin et al. (2017); Brock et al. (2019) and is referred to as an MLP scene function henceforth.

We further introduce an **attention-based** scene function, see Fig. 3 for an overview. Attention (Vaswani et al., 2017) allows using a high-dimensional spatial $[H_z \times W_z \times D_z]$ with latent variable over which inputs of the scene function can attend. The spatial structure arises from removing the final average pooling across locations in the ResNet encoder.⁵ Since the scene function is evaluated many times (e. g. 256 in Mildenhall et al. (2020); 128 in our experiments) for every pixel, it has to be computationally cheap with low memory footprint. Consequently, we use only one linear layer per attention block and no layer norm. Additionally, our attention blocks are bottlenecks, i.e. keys, queries and values are low dimensional c. f. Srinivas et al. (2021). We find that these choices are a good trade-off between computation, memory and capacity, and used throughout our experiments.

In order to model correlations between spatial locations, otherwise unaccounted for by an independent prior $p(\mathbf{z})$, we apply a small CNN to the latent before it is fed into the scene function, see Appendix B for further details.

4 Related Work

NeRF-VAE is closely related to amortized neural rendering approaches. Trevithick & Yang (2021); Yu et al. (2020) use

⁵Since the feature maps are averaged over context elements, locations in the latent do not necessarily correspond to parts of the scene; we use $H_z = W_z = 8$

NeRF as their decoder but require projecting all rendered points into the input space and thus do not formulate any compact scene representation. Tancik et al. (2020) suffers from a similar issue: it meta-learns good initializations for NeRF, but requires updating all parameters before it can render target observations. Sitzmann et al. (2019) uses sequential ray-marching instead of volumetric rendering, and demonstrates generalization only across objects from the same class. NeRF-VAE has many similarities with GQN of Eslami et al. (2018), with the difference that GQN uses a CNN for rendering and is therefore not necessarily consistent across views. Mescheder et al. (2019) show impressive single-image 3D reconstructions by modelling space occupancy with an implicit representation, though not modeling colours.

The above approaches work only when camera poses for input images are known. This is not true for GANs, where it is enough to approximate the marginal distribution of poses in the training set if appropriate inductive biases are in place (Nguyen-Phuoc et al., 2019)—an approach that also scales to an explicit multi-object setting (Nguyen-Phuoc et al., 2020). GRAF (Schwarz et al., 2020) and GIRAFFE (Niemeyer & Geiger, 2020) reuse the same idea for single- and multi-object settings, respectively, but use NeRF as the generator, which improves multi-view consistency. Both approaches are related to NeRF-VAE in the sense that they use NeRF as a decoder which is conditioned on a latent variable—although NeRF-VAE introduces a more advanced conditioning mechanism. Finally, in contrast to the GAN approaches, NeRF-VAE has an associated inference procedure.

A limitation of NeRF is that it can only model static scenes and does not support varying lighting conditions nor transient effects (e. g. moving objects) often visible in the real world. NeRF-w (Martin-Brualla et al., 2020) addresses these shortcomings by adding per-view latent variables. While our model makes latent variables explicit, it maintains a single latent per scene; an extension towards NeRF-w is an interesting research direction. Pumarola et al. (2020); Park et al. (2020); Du et al. (2020); Li et al. (2020); Xian et al. (2020) further extend NeRF to dynamic scenes and videos: they formulate flow-fields that augment the original radiance field with a temporal component. This complicated approach is necessary due to the high-dimensional nature of NeRF’s representation. Since NeRF-VAE introduce a latent variable, it is possible to extend it to videos by simply adding a latent dynamics model (e. g. Hafner et al. (2020)).

5 Experiments

To evaluate NeRF-VAE, we first analyze its ability to reconstruct novel viewpoints given a small number of input views, and contrast that with NeRF. Second, we compare our model with a Generative Query Network-like autoregressive

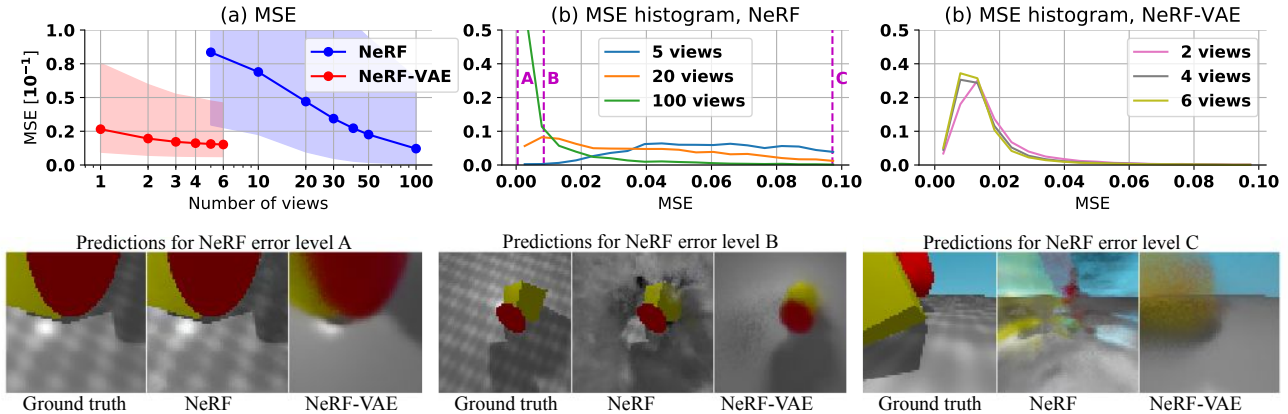


Figure 4: Error analysis of NeRF and a minimalistic version (see text) of NeRF-VAE on Jaytracer data. **(a)**: MSE decreases with increasing number of training (NeRF) and context (NeRF-VAE) views. We show the mean and 95% percentiles across 100 test views averaged over 10 scenes and 10 seeds. Despite its minimal version, NeRF-VAE performs much better for fewer (≤ 6) views; NeRF needs many more views (≥ 100) to reach comparable error. **(b, c)**: MSE histograms. Compared to NeRF-VAE, NeRF needs a large number of training views to consistently achieve low errors, and even then incurs a small number of larger errors. **Bottom**: An example scene, where views correspond to three error levels, indicated in (b), of NeRF trained on 100 views. NeRF’s predictions for level A are near perfect, but the model fails catastrophically for level C—which regularly happens when training on fewer views, see (b). NeRF-VAE’s predictions are more consistent, despite its simple decoder and inference.

convolutional model, (Eslami et al., 2018, GQN) and show that while NeRF-VAE achieves comparably low reconstructions errors, it has a much improved generalization ability, in particular when being evaluated on camera views not seen during training. Third, we provide an ablation study of NeRF-VAE variants, with a focus on the conditioning mechanisms of the scene function described in Section 3.2. Finally, we showcase samples of NeRF-VAE.

5.1 Datasets

We use three datasets, each consisting of 64×64 coloured images, along with camera position and orientation for each image, and camera parameters used to extract ray position and orientation for each pixel.

GQN (Eslami et al., 2018)⁶, consists of 200k scenes each with 10 images of rooms with a variable number of objects. Camera positions and orientations are randomly distributed along a plane within the rooms, always facing the horizon. Note that this dataset does not contain reflections or specularities, which we discuss in Section 5.4

CLEVR We created a custom CLEVR dataset (Johnson et al., 2017) with 100k scenes, each with 10 views. Each scene consist of one to three randomly coloured and shaped objects on a plane. Camera positions are randomly sampled from a dome. Orientations are such that all objects are always present, making inference from a limited number of

⁶We use the `rooms_free_camera_no_object_rotations` variant publicly available at <https://github.com/deepmind/gqn-datasets>

views easier than in the GQN data. The dataset is of higher visual quality than GQN, e. g. it includes reflections.

Jaytracer In order to have more control over individual aspects of the data (e. g. complexity, distribution of camera views, etc.), we also created a custom raytraced dataset which consists of 200k randomly generated scenes, each with 10 views, with a fixed number of objects in random orientations on a plane. Shapes, colours, textures, and light position are random, an example can be seen in Fig. 4.

For both CLEVR and Jaytracer, we generate 10 additional scenes each with 200 views and ground-truth depth maps for evaluation purposes and for training NeRF. See Appendix A for more details.

5.2 Implementation details

The conditional scene functions’ architecture follows NeRF, first processing position \mathbf{x} to produce volume density and then additionally receiving orientation \mathbf{d} to produce the output colours. Both position and orientation use circular encoding whereby we augment the network input values with a Fourier basis, c. f. Fig. 3.

We follow Mildenhall et al. (2020, Section 5.2) in using hierarchical volume sampling in order to approximate the colour of each pixel. This means we maintain a second instance of the conditional scene function (conditioned on the same latent \mathbf{z}), which results in an additional likelihood term in the model log-likelihood in Eq. (2).

We use Adam (Kingma & Ba, 2014) and β -annealing of the

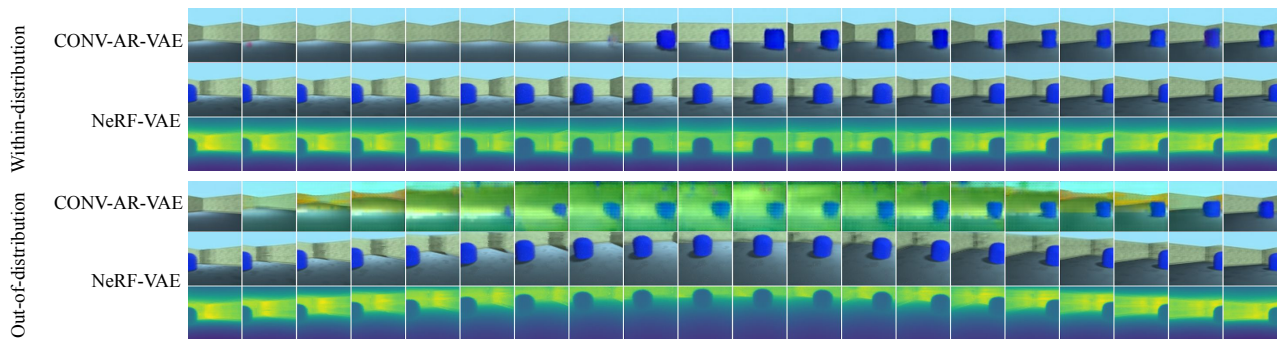


Figure 5: Generalization ability for interpolations along two trajectories. **Top**: the camera is moving parallel to the ground, facing the horizon (**within-distribution (WD)**), both models were trained using such views). While convolutional autoregressive VAE (CONV-AR-VAE) predicts the room consistently, it is inconsistent regarding the presence of the blue object. In contrast, NeRF-VAE produces fully consistent predictions, as further illustrated by visualizations of its inferred scene geometry. **Bottom**: the camera is further lifted off the ground, along a quadratic curve, facing downwards (**out-of-distribution (OOD)**). CONV-AR-VAE fails to account for downward camera orientations and outputs distorted colours, whereas NeRF-VAE produces plausible and consistent predictions and scene geometry.

KL term in Eq. (2). Full details can be found in Appendix B.

5.3 Comparison with NeRF

NeRF-VAE, unlike NeRF, can infer scene structure without re-training—through the introduction of a per-scene latent variable and shared across-scene parameters. Our first experiment explores the following questions: 1. Can NeRF-VAE leverage parameter sharing to infer novel scenes from very few views? 2. Is NeRF-VAE’s capacity affected by having a much smaller scene representation (a latent variable instead of an MLP). 3. At what number of views do both models reach comparable errors?

To focus on these conceptual differences between NeRF and NeRF-VAE, we use NeRF-VAE with the simple MLP scene function and without iterative inference. We train NeRF-VAE on the Jaytracer data using $N_{\text{ctx}} = 4$ context images (with corresponding cameras). We evaluate on 10 held-out scenes, with an increasing number of context views $N_{\text{ctx}}^{\text{test}} = 1, \dots, 6$.

We train a separate instance of NeRF on each of these same 10 evaluation scenes, with an increasing number of training views $5, \dots, 100$. Both models are evaluated on images of 100 unseen views from the 10 evaluation scenes. We train and evaluate both models using 10 different seeds. See Appendix E for further training details.

RESULTS

Fig. 4 (a) shows reconstruction MSEs (mean and 95% percentiles) across the 100 test views. NeRF-VAE achieves a significantly lower MSE and uniformly lower worst case errors compared to NeRF trained on less than 100 views. This is despite NeRF-VAE’s amortized inference, which is many orders of magnitude faster than running the full optimization in NeRF. NeRF achieves lower MSE than our model

only when sufficient training data is available (here = 100 views). We emphasize that while NeRF-VAE was trained using $N_{\text{ctx}} = 4$ context views, the model generalizes well to different numbers of context views at test time.

Taking a look at the distribution of errors and the corresponding predictions in Fig. 4 (b, c), we see that NeRF’s MSE distributions are extremely wide when trained on fewer than 100 views. Even for 100 views, NeRF suffers from a long tail of large errors. NeRF-VAE’s errors concentrate on a small positive value for all evaluated $N_{\text{ctx}}^{\text{test}}$, with tails comparable to NeRF with 100 training views.

Fig. 4, bottom, shows predictions from both models on an example scene, for views corresponding to error levels attained by NeRF trained on 100 views: near-perfect (A), medium (B), and catastrophic (C), marked in Fig. 4 (b). NeRF’s A-level predictions are near perfect, but significantly deteriorate in error levels B, C. As seen above, however, NeRF consistently (but not exclusively) attains level A only when trained with 100 views. We stress that in these simple scenes, this effect is not⁷ due to incomplete scene coverage from a limited number of views—NeRF is simply not able to interpolate well between few training views. In contrast, NeRF-VAE captures the scene structure well on all error levels—though the simple version used here (MLP scene function, no iterative inference) misses high frequency details such as sharp object boundaries and textures. This suggests that while amortized inference from few views is possible, NeRF-VAE could benefit from a more expressive scene function and a better inference mechanism.

⁷Similar results, including catastrophic failures of NeRF trained with few views, can be obtained on CLEVR data where most of the scene is visible in all views, see Appendix E.1.

5.4 Comparison with a Convolution-Based Generative Model

Our next set of experiments compares NeRF-VAE to a CONV-AR-VAE—a model that is very closely related to GQN of Eslami et al. (2018), but with slight modifications to make it comparable to NeRF-VAE, see Appendix C for details.

Both NeRF-VAE and CONV-AR-VAE are able to infer novel scenes from few input images, and to subsequently synthesize novel views within those scenes. The key difference between the models is their decoder, responsible for rendering images given camera and latent scene representation: convolutional for CONV-AR-VAE and geometry informed for NeRF-VAE.

INTERPOLATIONS & GENERALIZATION

We first illustrate that NeRF-VAE’s explicit knowledge of 3D geometry allows it to generalize well to out-of-distribution camera positions and orientations compared to CONV-AR-VAE.

We train both NeRF-VAE and CONV-AR-VAE on the GQN dataset, using similar settings, which are detailed in Appendix E.2. For the this experiment, we restrict NeRF-VAE’s scene function’s access to orientations, which we will motivate below. For evaluation, we select a held-out scene and let each model infer the latent representation given the same $N_{\text{ctx}}^{\text{test}} = 4$ views. We pick two arbitrary views and generate a sequence of camera positions and orientations that interpolates between them⁸. We do this twice: once with a simple linear interpolation across the plane, changing only the yaw of the camera (**within-distribution (WD) views**), and once with the camera lifting off the plane, along a quadratic curve, and looking down, changing both pitch and yaw (**out-of-distribution (OOD) views**); see Fig. 13 in Appendix E.2 for an illustration. We note that out-of-distribution here means that these camera positions lie outside the support of the training data distribution.

Fig. 5 shows each models’ outputs along the within-distribution trajectories and out-of-distribution views trajectories. Both models produce plausible within-distribution interpolations, although CONV-AR-VAE has problems with object persistency. When evaluated on out-of-distribution views, CONV-AR-VAE completely fails to produce plausible outputs: ignoring the downward camera angle and instead distorting colours of the scene. In contrast, NeRF-VAE renders the inferred scene geometry properly from out-of-distribution viewpoints. Fig. 5 further shows depth estimates for NeRF-VAE’s outputs, revealing the inferred scene geometry. We provide more examples and out-of-distribution experiments on CLEVR in Appendix E.2.

⁸Note that the GQN dataset does not contain ground truth images for these interpolated views.

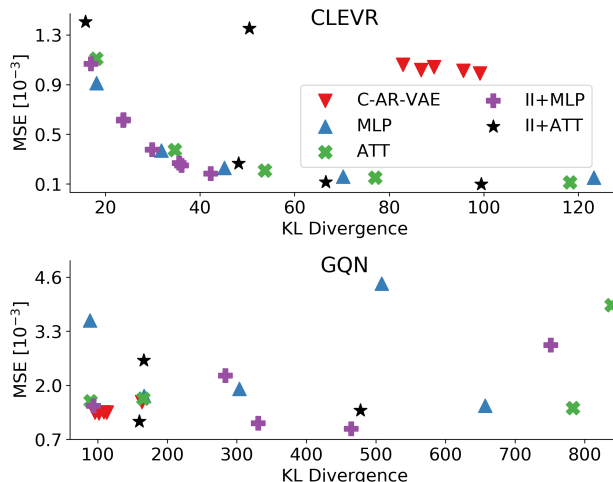


Figure 6: Variants of NeRF-VAE compared with CONV-AR-VAE on CLEVR and GQN datasets. We trained NeRF-VAE with a range of β values to investigate reconstruction/KL trade-offs. Iterative inference (II) improves MLP-based scene functions, but has a small effect on attentive (ATT) ones.

DEGENERATE ORIENTATIONS IN THE GQN DATA

Recall that camera views in the GQN data lie within a plane parallel to the ground. Consequently, certain points in the scene are **only** observed from orientations within this plane. When trained on this degenerate data, evaluating a neural-network-based scene function on different (e. g. when looking down) orientations inputs leads to unpredictable outputs. A simple way to circumvent the resulting rendering artifacts is to remove orientations from the scene function’s inputs, as done in the above interpolations. In the case of the GQN data, which does not contain viewpoint dependent colours (reflections or specularities), this restriction does not impair visual output quality. We replicate the interpolations from Fig. 5 with orientation inputs in Appendix E.3.

QUANTITATIVE COMPARISON & MODEL ABLATIONS

Fig. 6 shows MSE and Kullback-Leibler (KL)-divergence of NeRF-VAE variants using amortized or iterative amortized (II) inference and MLP or attentive (ATT) scene functions, and juxtaposes them against the CONV-AR-VAE. We focus on CLEVR and GQN datasets. All NeRF-VAEs are trained with increasing values of β to trace out the available trade-offs between MSE and KL. CONV-AR-VAE is trained with GECO (Rezende & Viola, 2018), which allows to set a user-specified constraint on the likelihood term, details in Appendix E.2.

CLEVR contains simple objects visible from every viewpoint, and has no complicated textures. Consequently, the MLP scene function achieves good MSE and KL. Iterative inference further increases reconstruction performance while decreasing KL. It is interesting that MLP-based models

tend to have lower KL values than attentive models while still maintaining good reconstruction. However, attentive models do obtain lower reconstruction errors in high-KL regimes, which suggests that they have higher capacity to model complicated data. CONV-AR-VAE is not able to model the CLEVR data well—the model attains high KL values despite manually setting a high MSE threshold.

The GQN dataset contains high-frequency textures and rooms which are not fully visible from every view, causing both a more difficult inference problem and more complicated rendering compared to CLEVR. The MLP scene function without iterative inference achieves low KL albeit generally higher MSE. ATT can achieve lower errors than MLP at similar KL levels, despite also reaching very large KL values, indicating a peaked posterior for certain values of β . Using iterative inference helps both decoders, and allows the model to achieve both lowest KL and MSE. We note that while CONV-AR-VAE achieves slightly lower MSE and KL on this within-distribution evaluation, it fails to generalize to out-of-distribution views as discussed above.

5.5 Samples & Uncertainty

We now demonstrate NeRF-VAE’s capability to learn an unconditional prior over scenes (as opposed to images).

We first sample the latent variable $z \sim p(z)$, and then render a number of views of the induced scene function $G_\theta(\cdot, z)$. Samples from NeRF-VAE trained on the GQN and CLEVR datasets are shown in Fig. 7. These samples resemble the training data distribution to a high degree, both in appearance and variability. Furthermore, the depth estimates (example in last row) reveal a consistent geometric structure of the sampled scene.

Fig. 8 shows an example where NeRF-VAE infers a scene from a single context image containing a barely-visible pink object. The model is able to accurately predict a view that contains the full object. At the same time, the model maintains uncertainty about the exact shape (sphere vs. icosahedron), as can be seen in the predictive variance of depth estimate.

6 Discussion

We presented NeRF-VAE, a geometry-aware scene generative model that leverages NeRF as a decoder in a VAE-framework. Thanks to an explicit rendering procedure, NeRF-VAE is view-consistent and generalizes to out-of-distribution cameras, unlike convolutional models such as GQN. Additionally, the learned prior over scene functions allows NeRF-VAE to infer scene structure from very few views. This is in contrast to NeRF, where too few views may result in contrived explanations of a scene that work for some views but not for others. The combination of geo-

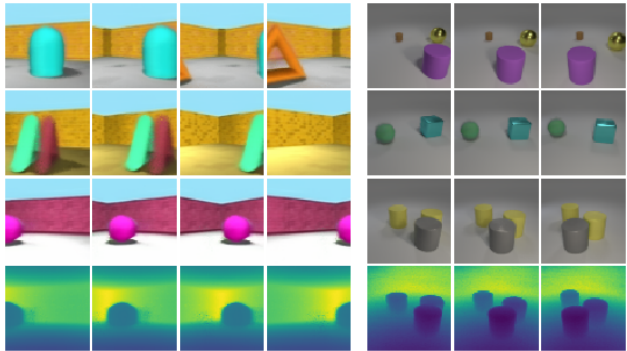


Figure 7: Sampled scenes from NeRF-VAE, trained on GQN (left) and CLEVR (right). Each row shows interpolated views in a different scene, corresponding to a sample of the latent variable. The last row shows a rendered depth map of the images in the above row (other depth maps omitted for space reasons).

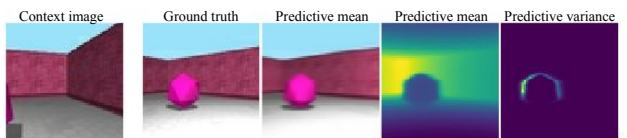


Figure 8: An example of predictions under limited information in the context view. We show colour and depth predictions. NeRF-VAE is able to reconstruct a plausible explanation of the object which is only marginally visible in the single context view. The predictive variance of depth estimates (averaged over 100 samples from the posterior over the latent variable) accounts for object boundaries not clearly visible in the context.

metric structure and a prior over scene functions, however, is not a panacea: if the data is degenerate (e. g. cameras restricted to a plane) and the model is overparameterized (e. g. unnecessarily accounting for view-dependent colours), NeRF-VAE might still explain the data in implausible ways.

One of the limitations of NeRF-VAE is its limited per-scene expressivity. NeRF allocates **all** of its capacity to a single scene, and is able to capture high levels of complexity. NeRF-VAE, however, splits its capacity between shared across-scene information (conditional scene function) and per-scene information (latent). In order to allow for amortized inference, the capacity of the latent needs to be limited—resulting in reduced per-scene expressivity compared to NeRF.

At the same time, a low-dimensional latent variable opens interesting possibilities for future work, e. g. interpolation between scenes, extensions to dynamic scenes and videos, and a latent representation that dynamically grows with input complexity.

References

- Brock, A., Donahue, J., and Simonyan, K. Large scale gan training for high fidelity natural image synthesis. In *International Conference on Representation Learning*, 2019.
- Cremer, C., Li, X., and Duvenaud, D. Inference Suboptimality in Variational Autoencoders. In *International Conference on Machine Learning*, 2018. arXiv/1801.03558.
- Curless, B. and Levoy, M. A volumetric method for building complex models from range images. In *Annual Conference on Computer graphics and Interactive Techniques*, pp. 303–312, 1996.
- Dai, A., Nießner, M., Zollöfer, M., Izadi, S., and Theobalt, C. BundleFusion: Real-time Globally Consistent 3D Reconstruction using On-the-fly Surface Re-integration. *ACM Transactions on Graphics*, 2017.
- Dosovitskiy, A., Springenberg, J. T., Tatarchenko, M., and Brox, T. Learning to Generate Chairs, Tables and Cars with Convolutional Networks. *IEEE Transactions on Pattern Analysis and Machine Intelligence*, 2014.
- Du, Y., Zhang, Y., Yu, H.-X., Tenenbaum, J., and Wu, J. Neural Radiance Flow for 4D View Synthesis and Video Processing. arXiv/2012.09790, 2020.
- Dumoulin, V., Shlens, J., and Kudlur, M. A Learned Representation For Artistic Style. In *International Conference on Representation Learning*, 2017. arXiv/1610.07629.
- Engel, J., Schöps, T., and Cremers, D. LSD-SLAM: Large-Scale Direct Monocular SLAM. In *European Conference on Computer Vision*, 2014.
- Engelcke, M., Kosiorek, A. R., Jones, O. P., and Posner, I. GENESIS: Generative Scene Inference and Sampling with Object-Centric Latent Representations. In *International Conference on Learning Representations*, 2019.
- Eslami, S. A., Rezende, D. J., Besse, F., Viola, F., Morcos, A. S., Garnelo, M., Ruderman, A., Rusu, A. A., Danihelka, I., Gregor, K., et al. Neural scene representation and rendering. *Science*, (6394):1204–1210, 2018. 360.
- Hafner, D., Lillicrap, T., Ba, J., and Norouzi, M. Dream to Control: Learning Behaviors by Latent Imagination. In *International Conference on Learning Representations*, 2020. arXiv/1912.01603.
- Hartley, R. and Zisserman, A. *Multiple view geometry in computer vision (2. ed.)*. 2003.
- He, K., Zhang, X., Ren, S., and Sun, J. Identity Mappings in Deep Residual Networks. In *European Conference on Computer Vision*, 2016. arXiv/1603.05027.
- Hu, J., Shen, L., Albanie, S., Sun, G., and Wu, E. Squeeze-and-Excitation Networks. *IEEE Transactions on Pattern Analysis and Machine Intelligence*, 42:2011–2023, 2020.
- Johnson, J., Hariharan, B., van der Maaten, L., Fei-Fei, L., Lawrence Zitnick, C., and Girshick, R. CLEVR: A Diagnostic Dataset for Compositional Language and Elementary Visual Reasoning. In *Conference on Computer Vision and Pattern Recognition*, July 2017.
- Kim, Y., Wiseman, S., Miller, A., Sontag, D., and Rush, A. M. Semi-Amortized Variational Autoencoders. In *International Conference on Machine Learning*, 2018.
- Kingma, D. P. and Ba, J. Adam: A method for stochastic optimization. arXiv/1412.6980, 2014.
- Kingma, D. P. and Welling, M. Auto-encoding variational bayes. In *International Conference on Learning Representations*, 2014.
- Levoy, M. and Hanrahan, P. Light field rendering. In *Annual Conference on Computer Graphics and Interactive Techniques*, pp. 31–42, 1996.
- Li, Z., Niklaus, S., Snavely, N., and Wang, O. Neural Scene Flow Fields for Space-Time View Synthesis of Dynamic Scenes. arXiv/2011.13084, 2020.
- Lowe, D. Distinctive Image Features from Scale-Invariant Keypoints. *International Journal of Computer Vision*, pp. 91–110, 2004. 60.
- Marino, J., Yue, Y., and Mandt, S. Iterative Amortized Inference. arXiv/1807.09356, 2018.
- Martin-Brualla, R., Radwan, N., Sajjadi, M. S., Barron, J. T., Dosovitskiy, A., and Duckworth, D. NeRF in the Wild: Neural radiance fields for unconstrained photo collections. arXiv/2008.02268, 2020.
- Mescheder, L. M., Oechsle, M., Niemeyer, M., Nowozin, S., and Geiger, A. Occupancy Networks: Learning 3D Reconstruction in Function Space. In *Conference on Computer Vision and Pattern Recognition*, pp. 4455–4465, 2019.
- Mildenhall, B., Srinivasan, P. P., Ortiz-Cayon, R., Kalantari, N. K., Ramamoorthi, R., Ng, R., and Kar, A. Local Light Field Fusion: Practical View Synthesis with Prescriptive Sampling Guidelines. *ACM Transactions on Graphics*, 2019.
- Mildenhall, B., Srinivasan, P. P., Tancik, M., Barron, J. T., Ramamoorthi, R., and Ng, R. NeRF: Representing Scenes as Neural Radiance Fields for View Synthesis. In *European Conference on Computer Vision*, 2020.

- Nguyen-Phuoc, T., Li, C., Theis, L., Richardt, C., and Yang, Y. HoloGAN: Unsupervised Learning of 3D Representations From Natural Images. In *International Conference on Computer Vision*, pp. 7587–7596, 2019.
- Nguyen-Phuoc, T., Richardt, C., Mai, L., Yang, Y., and Mitra, N. BlockGAN: Learning 3D Object-aware Scene Representations from Unlabelled Images. In *Advances in Neural Information Processing Systems*, 2020. arXiv/2002.08988.
- Niemeyer, M. and Geiger, A. GIRAFFE: Representing Scenes as Compositional Generative Neural Feature Fields. *arXiv/2011.12100*, 2020.
- Park, K., Sinha, U., Barron, J., Bouaziz, S., Goldman, D., Seitz, S., and Brualla, R.-M. Deformable Neural Radiance Fields. *arXiv/2011.12948*, 2020.
- Pumarola, A., Corona, E., Pons-Moll, G., and Moreno-Noguer, F. D-NeRF: Neural Radiance Fields for Dynamic Scenes. *arXiv/2011.13961*, 2020.
- Rezende, D. J. and Viola, F. Generalized ELBO with Constrained Optimization, GECO. In *NeurIPS Bayesian Deep Learning Workshop*, 2018.
- Rezende, D. J., Mohamed, S., and Wierstra, D. Stochastic Backpropagation and Approximate Inference in Deep Generative Models. In *International Conference on Machine Learning*, pp. 1278–1286, 2014.
- Schönberger, J. L. and Frahm, J.-M. Structure-from-Motion Revisited. In *Conference on Computer Vision and Pattern Recognition*, 2016.
- Schwarz, K., Liao, Y., Niemeyer, M., and Geiger, A. GRAF: Generative Radiance Fields for 3D-Aware Image Synthesis. *arXiv/2007.02442*, 2020.
- Sitzmann, V., Zollhöfer, M., and Wetzstein, G. Scene Representation Networks: Continuous 3D-Structure-Aware Neural Scene Representations. In *Advances in Neural Information Processing Systems*, 2019. arXiv/1906.01618.
- Srinivas, A., Lin, T.-Y., Parmar, N., Shlens, J., Abbeel, P., and Vaswani, A. Bottleneck Transformers for Visual Recognition. 2021.
- Srinivasan, P. P., Wang, T., Sreelal, A., Ramamoorthi, R., and Ng, R. Learning to Synthesize a 4D RGBD Light Field from a Single Image. In *International Conference on Computer Vision*, 2017.
- Tancik, M., Mildenhall, B., Wang, T., Schmidt, D., Srinivasan, P. P., Barron, J., and Ng, R. Learned Initializations for Optimizing Coordinate-Based Neural Representations. *arXiv/2012.02189*, 2020.
- Tatarchenko, M., Dosovitskiy, A., and Brox, T. Single-view to Multi-view: Reconstructing Unseen Views with a Convolutional Network. *arXiv/1511.06702*, 2015.
- Trevithick, A. and Yang, B. GRF: Learning a General Radiance Field for 3D Scene Representation and Rendering. In *International Conference on Learning Representations*, 2021. arXiv/2010.04595.
- Ulusoy, A. O., Black, M. J., and Geiger, A. Patches, Planes and Probabilities: A Non-Local Prior for Volumetric 3D Reconstruction. In *Conference on Computer Vision and Pattern Recognition*, pp. 3280–3289, 2016.
- Vahdat, A. and Kautz, J. NVAE: A Deep Hierarchical Variational Autoencoder. *arXiv/2007.03898*, 2020.
- Vaswani, A., Shazeer, N., Parmar, N., Uszkoreit, J., Jones, L., Gomez, A. N., Kaiser, Ł., and Polosukhin, I. Attention is all you need. *Advances in Neural Information Processing Systems*, pp. 5998–6008, 2017. 30.
- Xian, W., Huang, J., Kopf, J., and Kim, C. Space-time Neural Irradiance Fields for Free-Viewpoint Video. *arXiv/2011.12950*, 2020.
- Yu, A., Ye, V., Tancik, M., and Kanazawa, A. pixel-NeRF: Neural Radiance Fields from One or Few Images. *arXiv/2012.02190*, 2020.
- Zhou, T., Tucker, R., Flynn, J., Fyffe, G., and Snavely, N. Stereo magnification: learning view synthesis using multiplane images. *ACM Transactions on Graphics*, 2018.

NeRF-VAE: A Geometry Aware 3D Scene Generative Model

Supplementary Material

A Dataset Details

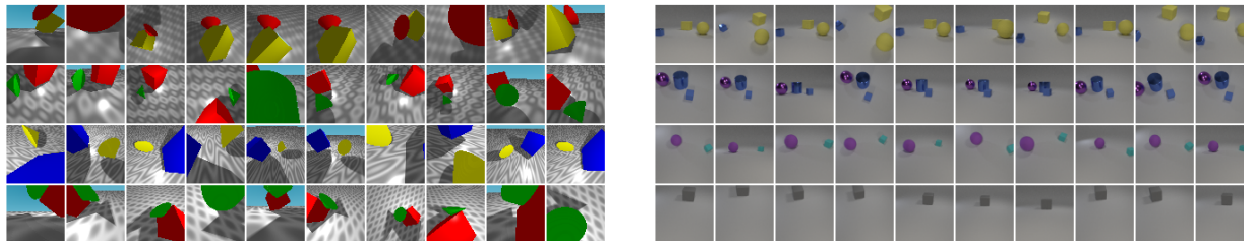


Figure 9: Multiple views (columns) of example scenes (rows) in the Jaytracer and CLEVR datasets. **Jaytracer** (left): This dataset has a much more diverse distribution of camera perspectives than both GQN and CLEVR—making scene inference more challenging. The example predictions in Fig. 4 are from the first scene shown here. **CLEVR** (right): Camera positions, angles and number of objects are randomized, compared to the original CLEVR data.

A.1 CLEVR

CLEVR (Johnson et al., 2017) is a widely used synthetic image dataset designed for visual reasoning. The generative process of a scene involves placing a number of objects of different shapes (cube, sphere, and cylinder), with randomly selected material properties, sizes, and positions on a ground plane, and random light positions. The camera is placed on a fixed location, $(7.48, -6.50, 5.34)$, with a small amount of random jitter added. We make a number of slight modifications that involve randomizing the camera pose and number of objects:

- The camera’s distance to the origin is uniformly sampled between $[6, 8]$,
- the elevation angle is shifted by an angle uniformly sampled between $[-20, 45]$,
- the azimuth angle is shifted by an angle uniformly sampled between $[-15, 40]$ degrees.
- Each scene is instantiated with one, two or three objects.

Examples are shown in Fig. 9

A.2 Jaytracer

The Jaytracer dataset was rendered using a customized raytracer written in Jax⁹. All scenes consist of an infinite ground plane, a dome acting as sky, and two objects. Ground textures are randomly generated for each scene, using a simple series linear operations and periodic nonlinearities, and a random colour within a range of gray-scales. The sky colour is random within a fixed range. Objects shapes and colours are randomly chosen from a fixed set (torus, box, sphere, cylinder, a set of 5 distinct colours), are randomly scaled within a given range, and randomly positioned within a rectangle around $(-1, 1)$ in the ground plane. Camera positions are uniformly sampled from a dome and oriented towards the origin. There is a single point source of white light, which is randomly placed within a box of a fixed size, along with a fixed level of ambient light. Scenes are represented as a collection of signed distance functions. We use a Lambert and a Blinn Phong Shader with a single pass of shadow rendering. Examples are shown in Fig. 9

⁹<http://github.com/google/jax>

B Architectural Details

B.1 Hierarchical sampling in NeRF

NeRF uses hierarchical sampling in the rendering process. First, a ‘coarse’ scene function is evaluated at various points along the rays corresponding to each image pixel. Second, based on the density values at these coarse points, a second set of points is re-sampled along the same rays, and a second ‘fine’ scene function (with the same architecture) is evaluated at the re-sampled points. The resulting (fine) densities and colours are used in NeRF’s volume rendering mechanism. In order to enable gradient updates of the coarse scene function (re-sampling implementation not differentiable), NeRF reconstructs pixel colours using both scene functions’ output, and minimizes a sum of the coarse and fine pixel errors. We follow this approach in all decoders of NeRF-VAE. This means that we maintain a coarse and a fine instance of the scene function network, and our likelihood in practice is

$$p_{\theta}(\mathbf{I} \mid \mathbf{z}, \mathbf{c}) = \prod_{i,j} \mathcal{N} \left(\mathbf{I}(i, j) \mid \hat{\mathbf{I}}_{\text{coarse}}(i, j), \sigma_{\text{lik}}^2 \right) \times \prod_{i,j} \mathcal{N} \left(\mathbf{I}(i, j) \mid \hat{\mathbf{I}}_{\text{fine}}(i, j), \sigma_{\text{lik}}^2 \right)$$

where $\hat{\mathbf{I}}_{\text{coarse}}(i, j)$, $\hat{\mathbf{I}}_{\text{fine}}(i, j)$ are the rendered images before and after the re-sampling step described above.

B.2 Encoder

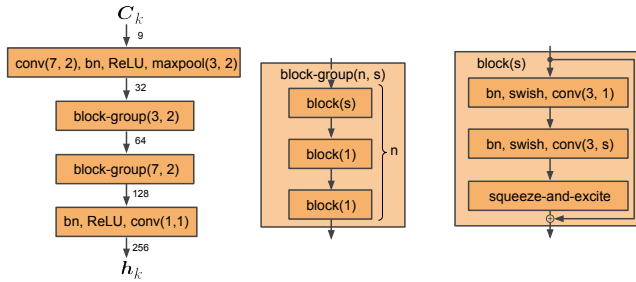


Figure 10: NouveauResNet adapted from Vahdat & Kautz (2020) and based on the ResNet v2 of He et al. (2016); bn stands for batch norm; ReLU and swish are activation functions. The arguments are (kernel size, stride) in conv(\cdot , \cdot) and maxpool(\cdot , \cdot), the number of blocks and the stride of the first block in block-group(\cdot , \cdot), and stride in block(\cdot). The numbers of channels are given next to the arrows. Convolutions do not use additive biases.

The approximate posterior $q_{\lambda}(\mathbf{z} \mid \mathbf{C})$ is conditioned on the context $\mathbf{C} = \{\mathbf{I}_k^{\text{ctx}}, \mathbf{c}_k\}_{k=1}^{N_{\text{ctx}}}$, which consists of images and associated camera position and orientation. We use the camera parameters to map \mathbf{c}_k into a 6-dimensional feature map containing positions of each pixel in \mathbf{I} (constant across one image), and the pixel’s corresponding ray orientation. We express orientations as a 3-dimensional unit vectors. We then concatenate the image $\mathbf{I}_k^{\text{ctx}}$ with the positions and orientation feature map to form a context element \mathbf{C}_k . The context elements are then encoded with a NouveauResNet derived from Vahdat & Kautz (2020), namely,

$$\begin{aligned} \mathbf{C}_k &= \text{concat}(\mathbf{I}_k^{\text{ctx}}, \text{map_to_rays}(\mathbf{c}_k)), \\ \mathbf{h} &= \frac{1}{N_{\text{ctx}}} \sum_{k=1}^{N_{\text{ctx}}} \text{NouveauResNet}(\mathbf{C}_k) \\ \lambda &= \text{MLP}(\mathbf{h}) \end{aligned} \quad (3)$$

where the final MLP is applied element-wise if \mathbf{h} is a feature map. Using λ , we obtain the posterior parameters by splitting λ into two parts for mean and standard deviation, where we use a softplus to ensure positivity of the latter.

The models that use the MLP scene function require a vector-valued latent \mathbf{z} . In this case we apply global average pooling on \mathbf{h} before it is fed into the MLP in Eq. (3). Attentive models use a feature-map-sized latent and do not require pooling in the encoder.

Iterative amortized inference For iterative inference, we approximate the ELBO loss (Eq. (2)) by subsampling a batch of pixels from images in the context (see also discussion below), and using that to calculate the gradient of the loss w.r.t. the posterior parameters λ . This gradient, together with \mathbf{h} , are then fed input to an LSTM, whose outputs are linearly mapped and added onto the current estimate of λ . Posterior parameters are obtained (from the final estimate of λ) as above.

Model	ELBO	MSE $[10^{-3}]$	KL	Model	ELBO	MSE $[10^{-3}]$	KL
Shift	3.73 \pm 0.051	2.53 \pm 0.344	703 \pm 12	Shift	3.84 \pm 0.050	1.76 \pm 0.331	692 \pm 5
Shift All	3.78 \pm 0.007	2.20 \pm 0.047	643 \pm 8	Shift All	3.87 \pm 0.008	1.59 \pm 0.052	661 \pm 7
AIN All	3.78 \pm 0.010	2.20 \pm 0.063	670 \pm 6	AIN All	3.88 \pm 0.006	1.54 \pm 0.035	660 \pm 7
Att	3.90 \pm 0.010	1.48 \pm 0.063	414 \pm 20	Att	3.97 \pm 0.027	1.06 \pm 0.172	345 \pm 16

(a) GQN data; scene function **without** orientation inputs.(b) GQN data; scene function **with** orientation inputs.

Table 1: Scene function ablations on the GQN dataset. Using orientation inputs in the scene function significantly improves performance but leads to overfitting on this dataset, c. f. Appendix E.3. We try to equalize KL of different models by setting different β values in the ELBO so that we can compare reconstruction errors directly.

Image encoder Our implementation of NouveauResNet follows the ResNet v2 of He et al. (2016) but uses swish activations and squeeze-and-excite (with the reduction ratio of 8, Hu et al. (2020)) modules as done by Vahdat & Kautz (2020).

B.3 Scene Functions

NeRF uses a multilayer perceptron (MLP) as its scene function. Similarly, we can form a conditional scene function G_θ by conditioning an MLP on \mathbf{z} as follows. Concatenate \mathbf{z} with the input point (\mathbf{x}, \mathbf{d}) (Shift). This is equivalent to setting a scene-specific bias in the first layer of F_θ . Concatenate \mathbf{z} with the inputs to all layers of G_θ (Shift All), which is equivalent to setting scene-specific bias vectors in all layers. Use \mathbf{z} to shift and scale inputs to all layers of G_θ (AIN all). This is similar to Adaptive Instance Norm (AIN) of Dumoulin et al. (2017), and translates to setting a scene-specific bias and performing column-wise scaling of the corresponding weight matrices of G_θ . Or we can use attention (Att) as described in Section 3.2. We compare these four options on the GQN data using scene function that either **do** or **do not use orientation inputs**. The results are available in Table 1. We used different β values in the ELBO to achieve similar KL values. Not surprisingly, increasing complexity of the conditioning mechanism leads to decreasing reconstruction errors, with the attentive scene functions of Section 3.2 achieving the best results.

Latent variable pre-processing We use a small MLP or CNN (in attentive scene functions) on the latent **before** it is fed into the scene function. Originally introduced to account for relations between locations in spatial latent variables as described in Section 3.2, this mechanism improves results in all models.

Fourier encoding We use $L = 10$ and $L = 4$ -component Fourier encoding for positions and orientations, respectively; see Fig. 3 for details.

C CONV-AR-VAE Baseline Details

The CONV-AR-VAE baseline used in our experiments is closely related to GQN of Eslami et al. (2018). We begin by describing the variant of the graphical model used in our experiments and highlighting differences with the original model. CONV-AR-VAE defines the following generative model

$$p_\theta(\mathbf{I}, \mathbf{z} \mid \mathbf{c}) = p_\theta(\mathbf{I} \mid \mathbf{z})p_\theta(\mathbf{z} \mid \mathbf{c}) \quad (4)$$

and the associated approximate posterior $q_\phi(\mathbf{z} \mid \mathbf{C}, \mathbf{c})$. The latent variable \mathbf{z} is composed of multiple latents $\mathbf{z}^i, i = 1, \dots, L$ generated in an autoregressive manner. Note that in contrast to our NeRF-VAE, both the prior and the posterior are conditioned on the camera \mathbf{c} , which results in a model that is **not** consistent across different views. This is because rendering an image from a different viewpoint requires re-sampling of the latent variable, and therefore changing the scene characteristics. The model **can** be consistent only when re-sampling from the posterior, when the posterior’s uncertainty is minimized by providing sufficient information in the context \mathbf{C} .

Graphical model differences In CONV-AR-VAE, the prior is conditioned on the camera but not on the context. The context is used only to condition the posterior. During training, we always reconstruct the same images that were provided in the posterior context \mathbf{C} , and we never condition the model on any additional images. The context **always** contains four distinct views of a scene. In contrast, GQN used a prior and likelihood conditioned on the prior context $\mathbf{C}_{\text{prior}}$, while the posterior was conditioned on a context $\mathbf{C}_{\text{posterior}}$ that contained the $\mathbf{C}_{\text{prior}}$ as well as additional images, and was always trained to reconstruct a single image from the posterior context. Both the prior and posterior contexts vary in size between minibatches, with occasionally empty prior context (in this case the model is equivalent to the baseline we used). The latter enables the model to sample scenes unconditionally.

Neural architecture of CONV-AR-VAE The posterior q_ϕ uses the same per-image encoder H_ϕ as NeRF-VAE, see Appendix B for details, with the difference that it uses $[(5, 2), (5, 1)]$ block groups (see Appendix B.2) for details. The prior and posterior both use an autoregressive process, implemented by a convolutional LSTM with kernel of size 5, 128 hidden units and 16×16 spatial dimensions. At each stage, the CONV-LSTM takes as input the latent \mathbf{z}_{i-1} from the previous stage concatenated with pre-processed camera (c.f. Appendix B) and the encoded context \mathbf{C} for the posterior. For the prior, the distribution parameters are computed by a single convolution with kernel of size 3 from the output of the prior CONV-LSTM. To compute the posterior, we take the prior distribution statistics, and we add a linear projection (from a CONV of kernel size 3) of the posterior CONV-LSTM outputs. All prior and posterior distributions are diagonal Gaussian. The latent variable at each stage is $16 \times 16 \times 16$, with $L = 7$ stages.

The latent variables are used to sequentially update a canvas of the same size as the image (in our case $64 \times 64 \times 3$). To do that, we use a transposed convolution with kernel size = stride = 4 and 128 channels, followed by a convolution with kernel of size 3 and 3 output channels, whose output is added to the canvas. Finally, the canvas is mapped to the mean of a Gaussian distribution with a fixed scale parameter of 0.1 by using a single per-pixel convolution. The model is trained with Generalized ELBO Constrained Optimization (GECO) (Rezende & Viola, 2018).

D Estimating the ELBO

NeRF-VAE, despite presented as a model of images, assumes conditional independence of the individual image pixels given the latent variable. Consequently, the model can be viewed as estimating the conditional probability of a single pixel given its corresponding ray in the camera’s image plane. This perspective is useful when discussing how to estimate the ELBO and to train with GECO, which we do below.

From image to pixel likelihood Let $\mathbf{c}(i)$ be a deterministic function of the camera \mathbf{c} and the pixel index i , mapping pixel index i to ray position and orientation (using the camera parameters, further discussed in Appendix B.2). A single pixel joint likelihood then is $p_\theta(\mathbf{I}(i), \mathbf{z} \mid \mathbf{c}(i)) = p_\theta(\mathbf{I}(i) \mid \mathbf{z}, \mathbf{c}(i))p(\mathbf{z})$. The resulting ELBO is equivalent to β -ELBO of image models when $\beta = 1/\text{num pixels}$. Therefore, we restore $\beta = 1$ by defining the likelihood term of NeRF-VAE as $p_\theta(\mathbf{I} \mid \mathbf{z}, \mathbf{c}) = \sum_{i=1}^{\text{num pixels}} p_\theta(\mathbf{I}(i) \mid \mathbf{z}, \mathbf{c}(i))$.

Monte Carlo approximation Since NeRF-VAE’s decoder allows reconstructing single pixels, it is possible to compute a unbiased estimate of the image likelihood as

$$\hat{p}_\theta(\mathbf{I} \mid \mathbf{z}, \mathbf{c}) \approx \frac{\text{num pixels}}{|S|} \sum_{s \in S} p_\theta(\mathbf{I}(s) \mid \mathbf{z}, \mathbf{c}(s)),$$

with S a set of pixels selected uniformly at random from the image \mathbf{I} . This is useful for NeRF-based models due to the expensive rendering process (the scene function is evaluated many times for every pixel). Moreover, one can trade-off a bigger batch size (of scenes) for a smaller number of pixels used in the estimate—a useful property, since in our early experiments a bigger batch size (with fewer pixels) resulted in quicker (wall-clock time) model convergence and increased final performance.

Using GECO to train pixel likelihood models An alternative to setting β manually is to use Generalized ELBO Constrained Optimization (GECO) (Rezende & Viola, 2018). GECO has shown excellent results in practice (Engelcke et al., 2019; Rezende & Viola, 2018). It works by putting an explicit constraint on the desired per-pixel-likelihood, which unifies training of pixel and image generative models. We use GECO to train our variant of GQN and the CONV-AR-VAE. However, applying GECO to NeRF-style models has its own issues: NeRF has two likelihood terms that are approximated with functions that are evaluated differently (Appendix B.1), requiring different manually-chosen constraint values. Instead, we opted for β -annealing with ELBO, which we use in all our experiments for NeRF-VAE.

E Experimental Details and Additional Results

E.1 Details: Comparison with NeRF

For training NeRF-VAE, we evaluate the ELBO of Eq. (2) by subsampling 512 rays and colours from the context images uniformly at random. We use a 128 dimensional latent variable, Adam with a learning rate of 5^{-4} for 10^6 iterations, and $\beta = 11-6$, which is annealed to 1^{-4} from iteration 40k to 140k. The decoder is the MLP scene function, with 4 layers with 64 units each for the both density and colour part, and a skip connection to layer two. Rays are evaluated within the interval

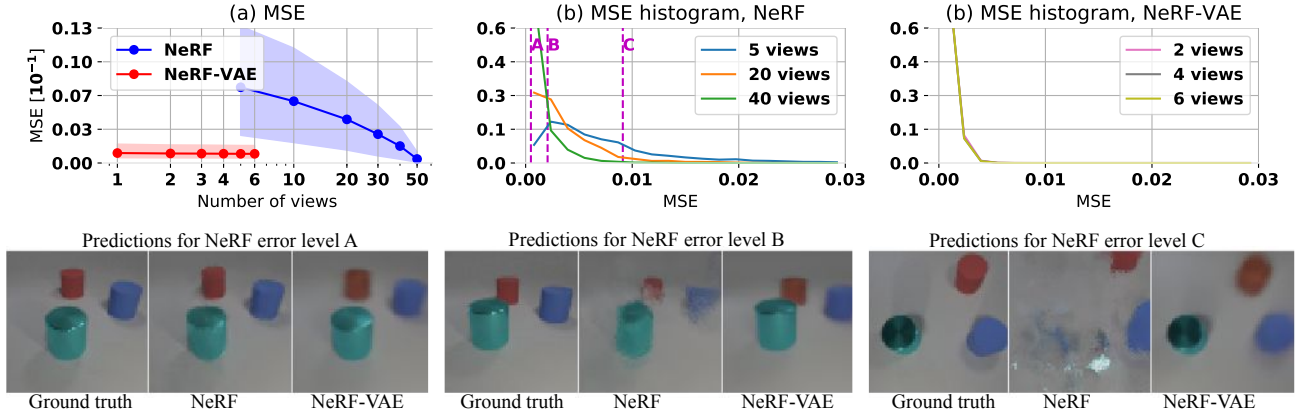


Figure 11: Error analysis of NeRF and a minimalistic version (MLP decoder, no iterative inference) of NeRF-VAE on CLEVR data. **(a)**: MSE decreases with increasing number of training (NeRF) and context (NeRF-VAE) views. We show the mean and 95% percentiles across 100 test views averaged over 10 scenes and 10 seeds. **(b, c)**: MSE Histograms. Compared to NeRF-VAE, NeRF needs a large number of training views to consistently achieve low errors, and even then incurs a small number of larger errors. **Bottom**: An example scene, where views correspond to three error levels, indicated in (b), of NeRF trained on 40 views.

$[0, 7]$, with 32 and 64 points for coarse and fine scene function respectively. As in Mildenhall et al. (2020), the densities are perturbed with Gaussian noise, but with smaller standard deviation of 0.01. In this version of NeRF-VAE, we do not apply a CNN to the latent variable. The encoder ResNet uses $[(5, 2), (5, 1)]$ block groups.

NeRF is trained with a batch size of 256 rays, using Adam with learning rate 1^{-3} , for 5^6 iterations. We use the same scene function architecture as for NeRF-VAE, but evaluate the rays on more points, 128 and 256 for coarse and fine respectively.

CLEVR DATA

In Section 5.3 we show the benefits of amortizing NeRF in the Jaytracer dataset in terms of view prediction errors as a function of the number of input views. We repeat the experiment on CLEVR data, using the same settings, apart from extending the ray intervals to $[0.05, 14]$.

We carry out the same experiment on our CLEVR dataset and test on a dataset of 10 scenes with 100 views per scene. We observe the same pattern again in Fig. 11 (a). In fact, in this case NeRF-VAE is able to perform well with just observing one view, and no further benefits are seen from having more views. This is because in CLEVR all objects are seen with one single image which allows the inference model to encode the whole scene. On the other hand, NeRF still suffers when it uses few views and it needs up to 50 views to get comparable MSE with NeRF-VAE. For example, when 20 views are used, there is still a heavy tail of prediction errors across the 100 views as seen in Fig. 11 (b). Upon closer inspection of the predictions, these large errors are often produced by views in which the camera has an extreme viewpoint (e.g. very high elevation, as shown in the error level C of Fig. 11), as these views are less likely to be within the range of input views.

E.2 Details: Comparison with a Convolution-Based Generative Model

We use the Adam optimizer (Kingma & Ba, 2014) with learning rate $= 3 \times 10^{-4}$ for Jaytracer and GQN datasets and $= 5 \times 10^{-4}$ for the CLEVR dataset. The batch size is 192 for NeRF-VAE and 256 for CONV-AR-VAE. The non-iterative NeRF-VAEs and CONV-AR-VAE are trained for 10^6 iterations and the iterative models are trained for 5×10^5 iterations (with 7 iterative inference steps). The β annealing starts at the beginning of training for GQN and after 20k iterations for CLEVR at a low value of β (0 for GQN, final $\beta/1024$ for CLEVR) and linearly increases across 100k iterations to the final value. The final β values were $[0.064, 0.256, 1.024, 4.096, 16.384]$ for GQN; for CLEVR these values were multiplied by a factor of 10. The iterative versions of NeRF-VAE estimate the image likelihood with a random sample of 256 pixels taken across the four target views; the non-iterative versions use 512 random pixels. CONV-AR-VAE is trained with GECO instead of β annealing to a likelihood threshold of 3.3, 3.95 and 4.0 on Jaytracer, GQN and CLEVR datasets, respectively.

All models use the encoder described in Appendix B with the following hyperparameters. All NeRF-VAEs use $[(3, 2), (7, 1)]$ block groups in the encoder; the CONV-AR-VAE uses $[(5, 2), (5, 1)]$ block groups. The latent z is a 128-dimensional vector

when the MLP scene function is used. For the attentive scene function we use $8 \times 8 \times 128$ feature map. The MLP used to predict the parameters of the posterior in Eq. (3) has 2 layers of 256 units each. We also apply an MLP or a CNN on the latent z before passing it into the scene function; the MLP has one layer of 256 on Jaytracer and GQN data and two layers of 128 units each on CLEVR. The attentive function use a CNN of three layers of 64 units each with kernel size 3 on all datasets.

The MLP scene functions use 2 density layers and 4 colour layers with 256 units each. The attentive scene function use 3 density layers and 3 colours layers with 256 units each. The final density and colour are predicted with a 2-layer MLP from the intermediate features.

E.3 Details: Interpolations & Generalization on GQN data

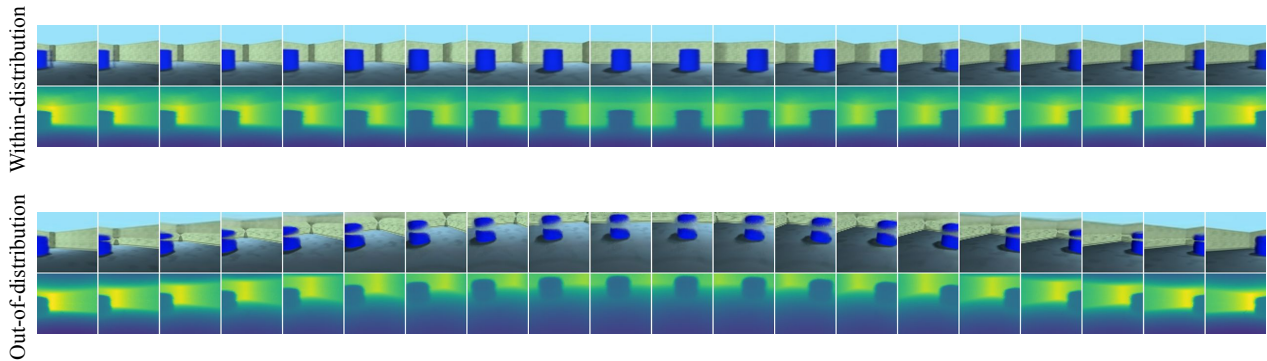


Figure 12: **Top:** View interpolations on GQN data with NeRF-VAE where the scene function has access to orientations. Within-distribution interpolations look as expected, but out-of-distribution evaluations suffer from colour artifacts (depth estimates are unaffected). Compare with Fig. 5 where the model has no access to orientations.

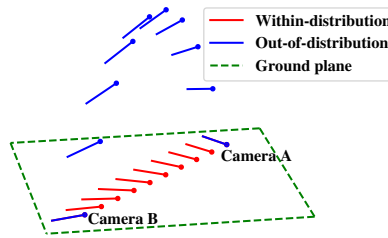


Figure 13: **Left:** Illustration for within and out-of-distribution camera trajectories for two representative cameras in the GQN dataset, used in Fig. 5. While within-distribution cameras are linear interpolations between the two endpoint positions and orientations within the ground plane, out-of-distribution cameras are additionally lifted of the ground and face downwards slightly.

Fig. 13 shows an illustration of how out-of-distribution camera trajectories are generated.

We replicate NeRF-VAE’s out-of-distribution interpolations from Fig. 5 with orientation inputs in Fig. 12. While within-distribution interpolations look as expected, the colours in the out-of-distribution interpolations are distorted—presumably as certain points in the scene function are evaluated at unseen orientations. Note that the densities, as depicted in the depth maps, are not affected by this problem, as densities are computed from positions only.

E.4 Generalization on CLEVR

We now investigate generalization on CLEVR data. We focus on two aspects: 1) Comparing NeRF-VAE to CONV-AR-VAE on out-of-distribution camera views, 2) comparing the attention-based scene function compared to the MLP on out-of-distribution number of objects.

Novel camera viewpoints As with the GQN data, we expect NeRF-VAE to also generalize better to unseen viewpoints in CLEVR compared to the convolutional baseline CONV-AR-VAE. To evaluate this we create a dataset with 20 scenes and 64 views. Four views are sampled as per the camera distribution of original training dataset, and used as the context views. The remaining 60 views are out-of-distribution, where 20 views interpolate between different elevations (at distance 4 to origin), 20 views where we interpolate between different azimuths (at distance 4 to origin) and 20 views where we interpolate distance to the origin between 2 and 6 (compared to sampled from [6, 8] during training). We train the (II+ATTN)-variant of NeRF-VAE and compare it with CONV-AR-VAE. Fig. 15 (left), and Fig. 14 (a) show that NeRF-VAE achieves higher quality image outputs, as also indicated by lower MSE and KL.

Number of objects We generate a test dataset (20 scenes, 60 views) that instantiates four or five objects instead of one to three in the training dataset. We train and compare NeRF-VAE with both the MLP and the attention-based scene function. Fig. 15 (right), and Fig. 14 (b) show that the attention-based scene function is able to generalize to larger number of objects,

whereas the MLP scene function misses objects. This also results in lower MSE. We hypothesize this attractive feature of the attentive scene function is due to its spatial latent representation—enabling the ability to handle objects in scenes irrespective of the spatial arrangement and quantity seen during training.

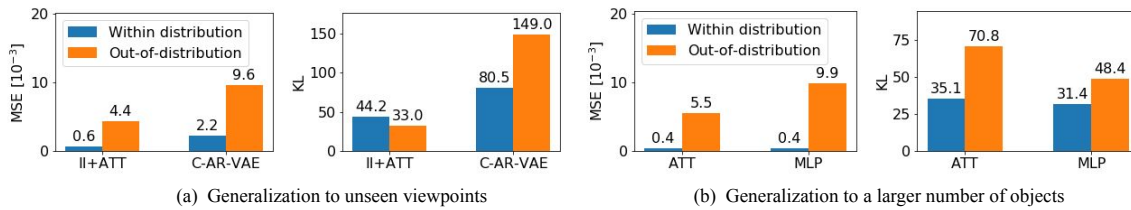


Figure 14: **(a)** Comparison of NeRF-VAE and CONV-AR-VAE on out-of-distribution camera viewpoints. NeRF-VAE obtains lower MSE and KL. **(b)** Comparison of MLP and ATTN scene functions on out-of-distribution number of objects. ATTN improves generalization. Median MSE and KL over 5 seeds.

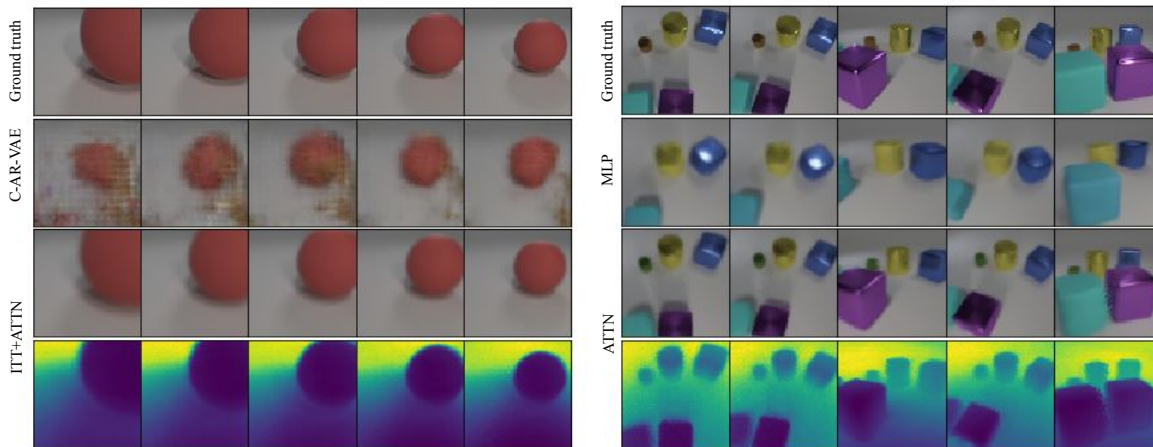


Figure 15: **Left:** Generalization to out-of-distribution camera views. While CONV-AR-VAE fails to produce plausible predictions, NeRF-VAE generalizes well. **Right:** Generalization to larger number of objects. The MLP scene function misses objects, while ATTN captures all objects.